

# Photon statistics and speckle visibility spectroscopy with partially coherent X-rays

Luxi Li,<sup>a\*</sup> Paweł Kwaśniewski,<sup>b</sup> Davide Orsi,<sup>c</sup> Lutz Wiegart,<sup>a</sup> Luigi Cristofolini,<sup>c</sup> Chiara Caronna<sup>d</sup> and Andrei Flueraș<sup>a</sup>

<sup>a</sup>Photon Sciences Directorate, Brookhaven National Laboratory, Upton, NY 11973, USA,

<sup>b</sup>European Synchrotron Radiation Facility, BP 220, F-38043 Grenoble, France, <sup>c</sup>Department of Physics and Earth Sciences, University of Parma, Parma, Italy, and <sup>d</sup>Stanford Linear Accelerator Laboratory, Menlo Park, CA 94025, USA. \*E-mail: luxi.li2012@gmail.com

A new approach is proposed for measuring structural dynamics in materials from multi-speckle scattering patterns obtained with partially coherent X-rays. Coherent X-ray scattering is already widely used at high-brightness synchrotron light sources to measure dynamics using X-ray photon correlation spectroscopy, but in many situations this experimental approach based on recording long series of images (*i.e.* movies) is either not adequate or not practical. Following the development of visible-light speckle visibility spectroscopy, the dynamic information is obtained instead by analyzing the photon statistics and calculating the speckle contrast in single scattering patterns. This quantity, also referred to as the speckle visibility, is determined by the properties of the partially coherent beam and other experimental parameters, as well as the internal motions in the sample (dynamics). As a case study, Brownian dynamics in a low-density colloidal suspension is measured and an excellent agreement is found between correlation functions measured by X-ray photon correlation spectroscopy and the decay in speckle visibility with integration time obtained from the analysis presented here.

## 1. Introduction

With the advent of high-brightness third-generation synchrotron radiation sources, X-ray photon correlation spectroscopy (XPCS) has become a widely used method for the study of mesoscale and nanoscale dynamics in a wide variety of materials [*e.g.* Sutton (2008) and Grübel *et al.* (2008), and references therein]. Key for XPCS is an illumination of the sample with partially coherent X-rays obtained by sufficiently collimating the radiation from a chaotic synchrotron radiation source, which leads to the appearance of ‘speckles’ in the scattering patterns (Sutton *et al.*, 1991). With a dynamic sample, the speckles fluctuate in time and the characteristic timescales associated with the relaxation mechanisms can be measured from the intensity autocorrelation functions. If combined with area detectors and a multi-speckle technique, XPCS can be used to measure both equilibrium and non-equilibrium dynamics (Sutton *et al.*, 2003).

Currently, XPCS enables studies of dynamics on timescales from milliseconds to seconds or longer (Grübel *et al.*, 2008). Limited by the available coherent flux or, in many cases, by detector technology, the applications of XPCS to faster dynamics on milliseconds and shorter timescales are restricted to only a few studies [*e.g.* Sikhharulidze *et al.* (2002)]. With the

development of modern high-brightness third-generation synchrotron radiation sources such as the National Synchrotron Light Source II (NSLS-II) at Brookhaven National Laboratory and fourth-generation X-ray free-electron lasers such as the Linear Coherent Light Source at Stanford Linear Accelerator Laboratory (SLAC), more photons than was ever possible before can be delivered to the sample in a short period of time enabling, in principle, studies of much faster dynamics. However, in order to do this, other instrumental limitations, such as the relatively slow readout speed of ‘fast’ pixelated area detectors reaching today frame repetition rates of about 1 kHz for state-of-the-art instruments (Ponchut *et al.*, 2011; Radicci *et al.*, 2012), need to be overcome first. While the development of faster (and smarter) pixelated area detectors is, and should remain, one of the highest priorities in synchrotron science, there is a pressing need for new experimental techniques pushing the limits towards measuring dynamics on shorter timescales with existing detectors. Speckle visibility spectroscopy (SVS) was introduced to laser light scattering (Bandyopadhyay *et al.*, 2005) and applied to measure fast changes associated with fluidization in a periodically driven granular system (Dixon & Durian, 2003). In SVS, the dynamics are measured from single diffraction patterns by quantifying the speckle contrast (or ‘speckle

visibility') as a function of integration time. With a dynamic sample, the speckles will appear 'blurred' as the integration time increases, and the dynamic timescales can be evaluated from the decay in speckle visibility with increasing integration times. An important advantage of SVS is the fact that it can give access to dynamics faster than the repetition rate of the detector as long as the integration time can be controlled on these shorter timescales (*e.g.* by a fast shutter).

A major obstacle encountered in applying SVS to coherent X-ray scattering is the low scattering intensity. Indeed, the standard SVS analysis (Bandyopadhyay *et al.*, 2005), where the speckle contrast is calculated as the normalized variance of the speckle patterns over an ensemble of equivalent pixels, fails here. In many cases, and most predominantly for speckle patterns recorded with short integration times, the presence of fake dark speckles increases the normalized variance, which seems greater than the actual contrast.

The first example of X-ray speckle visibility spectroscopy (XSVS) was demonstrated by Inoue *et al.* (2012), where the scattering of a Brownian sample was measured by a fast charge-coupled device (CCD) X-ray camera. In order to mitigate artifacts resulting from the low scattered intensity and from charge-sharing among adjacent pixels, the authors had to introduce an empirical fitting parameter in the expression describing the normalized variance of intensity fluctuations from speckle statistics and (Poisson) noise in the detection system. Later, another research group (DeCaro *et al.*, 2013) measured the short-time dynamics of a colloidal suspension by controlling the exposure time of a slow direct-illumination CCD camera by means of a fast mechanical shutter (a tuning fork). In order to overcome problems related to detection noise in the CCD detectors, the authors used a numerically intensive algorithm running on a supercomputer to calculate the spatial correlation of intensity fluctuations between adjacent pixels in an experimental set-up where the speckles were magnified through focusing and were larger than the detector pixel size. While this method can be extremely powerful in measuring fast dynamics in very low scattering systems, it is clearly quite difficult to be used on a routine basis.

As an alternative approach, here we use noiseless photon-counting pixelated area detectors which are becoming the standard for coherent X-ray scattering experiments; see, for example, the Maxipix and Eiger developments (Ponchut *et al.*, 2011; Gimenez *et al.*, 2011; Ballabriga *et al.*, 2013; Radicci *et al.*, 2012). As the signal is discriminated and converted to single photon counts for each pixel individually, this leads to much faster and less noisy devices, where the exposure time is typically controlled to the microsecond level by an electronic shutter. The intensity fluctuations over a set of equivalent pixels is described by the negative-binomial distribution function (see §2), taking into account speckle statistics associated with the partial coherent illumination and Poisson noise in the detection system. Here we show that this method and model work remarkably well with the data recorded with a fast pixelated detector, making the XSVS analysis rather straightforward, free of any empirical parameters, and readily

available to the entire synchrotron radiation user community. A similar approach was also used to demonstrate the presence of speckle in low-scattering patterns obtained from the scattering of single pulses from the X-ray free-electron laser source at SLAC (Hruszkewycz *et al.*, 2012; Lee *et al.*, 2013).

In addition to giving access to faster dynamics compared with more traditional methods such as XPCS, XSVS has another major advantage in reducing the risk of beam-induced sample damage. As long as nominally the same measurement can be reproduced on a new sample, or a fresh location of an irradiated sample, an ensemble can be built by repeating the same single-shot experiment until the desired signal-to-noise ratio is achieved.

In this paper we demonstrate for the first time the photon statistics approach to the XSVS method at high-brightness synchrotron radiation facilities by measuring the dynamics of a diluted colloidal suspension of hard-sphere silica particles undergoing Brownian motion. The sample does not show any signs of beam damage. The photon statistics approach is quite general and applicable to all illumination conditions, and we demonstrate a complete overlap between XSVS and XPCS results. A systematic experimental protocol is suggested for XSVS applied in third-generation synchrotron radiation sources.

## 2. Theory

In XPCS, the equilibrium sample dynamics are measured by the autocorrelation function of the scattered intensity  $I(t)$  from the illumination with (partially) coherent X-rays, given by

$$g^{(2)}(q, \tau) \equiv \frac{\langle I(q, t)I(q, t + \tau) \rangle}{\langle I(q, t) \rangle^2}, \quad (1)$$

where  $\langle \dots \rangle$  represents an ensemble average over nominally equivalent pixels and a time average over all the equivalent times  $t$ ,  $q$  is the scattering vector and  $\tau$  is the time delay. Assuming Gaussian statistics (which apply to most practical situations), the intensity autocorrelation  $g^{(2)}(q, \tau)$  is connected to the intermediate scattering function (ISF)  $g^{(1)}(q, \tau)$ , which contains the dynamical information of the sample motion, *via* the Siegert relation,

$$g^{(2)}(q, \tau) = \beta_1 [g^{(1)}(q, \tau)]^2 + g_\infty. \quad (2)$$

Here  $\beta_1$  is the optical contrast and is usually equal to the contrast factor of the speckle patterns in XPCS measurements, and  $g_\infty$  is the baseline, which is equal to 1 for ergodic samples. For a system undergoing diffusive dynamics, the ISF is described by  $g^{(1)}(q, \tau) = \exp[-\gamma(q)\tau]$ , where  $\gamma(q)$  is the relaxation rate associated with the sample dynamics. The autocorrelation function [equation (2)] can then be rearranged into

$$g^{(2)}(q, \tau) = \beta_1 \exp[-2\gamma(q)\tau] + g_\infty. \quad (3)$$

For XSVS, the theoretical framework is described by the semi-classical model following the work of Mandel (1958, 1959). Firstly, we summarize the formalism introduced by Bandyo-

padhyay *et al.* (2005) for SVS with laser light, which is based on the statistical wave measure of the scattered intensity  $I(t)$ . In reality, the time-resolved continuous scattering intensity  $I(t)$  cannot be measured with infinite resolution. Instead, the integrated signal  $\tilde{I}(t, T)$  of duration  $T$  is used from the recording of a detector, or

$$\tilde{I}(t, T) = \alpha \int_t^{t+T} I(t') dt', \quad (4)$$

where  $\alpha$  is a constant representing the detector efficiency. The time and spatial average (for multi-speckle techniques) of  $\tilde{I}(t, T)$  gives  $\langle \tilde{I}(T) \rangle$ . As in SVS (Bandyopadhyay *et al.*, 2005), the speckle patterns are usually recorded with a highly coherent high-intensity incident beam making the intensity fluctuations quasi-continuous and spanning a large dynamic range. In this intense beam condition, the classical particle behavior (photoelectrons as discrete particles) of the detection process, or the shot noise, is negligible, and the signal is fully described by the statistics of classical waves. Therefore, the probability density  $P(\tilde{I})$  is approximated by a gamma distribution function (Mandel, 1959),

$$P(\tilde{I}) = \left( \frac{M}{\langle \tilde{I} \rangle} \right)^M \frac{\tilde{I}^{M-1}}{\Gamma(M)} \exp\left(-M \frac{\tilde{I}}{\langle \tilde{I} \rangle}\right), \quad (5)$$

where  $M$  is the number of coherent modes of the integrated scattered signals, and  $\Gamma(\dots)$  is the gamma function. The contrast factor  $\beta$  of detected signals is defined as

$$\beta = 1/M. \quad (6)$$

When the (partially) coherent X-ray beam impinges on a sample, the degeneracy is increased by the disorder of the sample as well as the motion of the scatterers. Therefore, the number of coherent modes  $M$  increases, which results in a decrease in the contrast factor  $\beta$ . The moment analysis of the photon statistics leads to the normalized variance of the integrated signals  $\text{var}_{\tilde{I}}$ , given by

$$\text{var}_{\tilde{I}} = \langle \tilde{I}^2 \rangle / \langle \tilde{I} \rangle^2 - 1. \quad (7)$$

$\text{var}_{\tilde{I}}$  is related to the contrast factor  $\beta$ , or the number of coherent modes  $M$  through the probability density functions. For signals  $\tilde{I}$  following the gamma distribution,  $\text{var}_{\tilde{I}}$  is equal to the contrast factor  $\beta$  (Mandel, 1958, 1959),

$$\text{var}_{\tilde{I}}(q, T) = \beta(q, T). \quad (8)$$

In SVS, the experimental contrast factor  $\beta(q, T)$  is calculated by the normalized variance  $\text{var}_{\tilde{I}}$  of the speckle patterns (Bandyopadhyay *et al.*, 2005). The above approach is also applicable to XSVS as long as the scattered signal is intense enough, so that the gamma distribution holds.

In theory, the contrast factor can be written as a function of the ISF (Mandel, 1958; Bandyopadhyay *et al.*, 2005) under the Gaussian wave assumption,

$$\beta(q, T) = \beta_1 \int_0^T 2(1 - t/T) [g^{(1)}(q, t)]^2 dt / T + \beta_\infty, \quad (9)$$

where  $\beta_\infty$  is the baseline and is usually equal to 0. Numerically,  $\beta_1$  is the contrast factor of the speckle patterns obtained in the

shortest integration time in the XSVS measurements. When the integration time is much shorter than the sample relaxation timescale, then  $\beta_1$  is equal to  $\beta_0 = \lim_{T \rightarrow 0} \beta(T)$  for both XSVS and XPCS. The dynamic information of the sample motions is extracted by fitting the experimental  $\beta(q, T)$  with equation (9).

So far we have been describing the theory in terms of the statistics of classical waves. However, it is well known that when the scattering intensity is low the discrete nature of the scattered radiation will be significant and even dominant. In this case the signal is depicted as the number of events or counts  $K$ . The probability density function  $P(t, T, K)$ , which denotes the probability of detecting  $K$  counts in the time interval from  $t$  to  $t + T$  with a given integrated intensity  $\tilde{I}(t, T)$ , follows the Poisson distribution (Mandel, 1958),

$$P(t, T, K) = \frac{[\tilde{I}(t, T)]^K}{K!} \exp[-\tilde{I}(t, T)]. \quad (10)$$

Therefore, the probability density of photon events  $K$  for a given integration time  $T$  is the average of equation (10) over an ensemble of  $\tilde{I}$ . The resulting form is the negative-binomial distribution function (Mandel, 1959; Goodman, 2007)

$$P(K) = \frac{\Gamma(K + M)}{\Gamma(K + 1)\Gamma(M)} \left( \frac{M}{\langle K \rangle + M} \right)^M \left( \frac{\langle K \rangle}{M + \langle K \rangle} \right)^K, \quad (11)$$

which is a convolution of the gamma and the Poisson distributions. The moment analysis of the negative-binomial distribution gives a normalized variance  $\text{var}_K$  (Mandel, 1959),

$$\text{var}_K(q, T) = \beta(q, T) + \frac{1}{\langle K(q, T) \rangle}. \quad (12)$$

Equation (12) deviates from equation (8) or the speckle contrast  $\beta(q, T)$  by the term of the mean count  $\langle K \rangle$ . When  $\langle K \rangle$  is large, the photon beam is semi-continuous. As a result, the signal variation  $\text{var}_K$  (the quantal measure of the intensity) is identical to  $\text{var}_{\tilde{I}}$  (the classical wave measure). The negative-binomial distribution also reduces to the gamma distribution. On the other limit of low degeneracy when  $\langle K \rangle$  is small, the signal variance is dominated by the particle property of the beam and the classical Poisson distribution is recovered. Therefore, the negative-binomial distribution is applicable to all intensity levels in XSVS experiments, and the contrast factor  $\beta$  (or  $1/M$ ) can be determined directly in all cases by fitting the probability density of photon counts from the experimental XSVS results to the negative-binomial distribution [equation (11)]. The dynamic information is then extracted from the contrast factor at different integration time  $T$  using equation (9).

Depending on the exact nature of the dynamical process taking place, equation (9) leads to various analytic expressions (Bandyopadhyay *et al.*, 2005). For samples undergoing a diffusive motion, equation (9) becomes

$$\beta(q, T) = \beta_1 \frac{\exp[-2\gamma(q)T] - 1 + 2\gamma(q)T}{2[\gamma(q)T]^2} + \beta_\infty. \quad (13)$$

### 3. Experiment

The coherent X-ray scattering was performed at the ID10A beamline Tröika at the European Synchrotron Radiation Facility (ESRF) in Grenoble, France. A single-bounce Si(111) crystal monochromator was used to tune the X-ray energy to 8 keV with a relative bandwidth of  $\Delta\lambda/\lambda \simeq 10^{-4}$ . Higher-order X-rays were removed by a Si mirror placed downstream of the monochromator. A transversely partial coherent beam was tailored to a spot size of  $10 \mu\text{m} \times 10 \mu\text{m}$ , using beryllium compound refractive lenses and beam-defining slits. A set of guard slits was placed just upstream of the sample to block the diffraction fringes from the beam-defining slits. Under these conditions, the partially coherent X-ray flux was  $\sim 10^{10}$  photons  $\text{s}^{-1}$ . The scattered light was recorded using a Maxipix photon-counting detector (Ponchut *et al.*, 2011) with  $55 \mu\text{m} \times 55 \mu\text{m}$  pixel size located 2.2 m downstream of the sample. The sample-to-detector distance was adjusted to match the speckle size to the pixel size and optimize the optical contrast (Bandyopadhyay *et al.*, 2005). A vacuum flight path with kapton windows on both ends was installed between the sample and the detector to reduce air absorption and scattering.

The sample was prepared from a suspension of charge stabilized colloidal silica spheres (purchased from Duke Scientific, radius 250 nm) by replacing the initial solvent (water) with propylene glycol (PG). The concentration of the suspension was kept low ( $<2\%$ ) in order to reduce inter-particle correlations (Orsi *et al.*, 2012). As a consequence the colloids could diffuse freely, which is a good model system for Brownian motion. The colloidal suspensions were filled in 1 mm quartz capillaries and placed in a temperature-controlled SAXS chamber to keep the sample temperature at 285 K throughout the data acquisition. As this sample does not present any signs of beam damage, the speckle patterns were recorded repeatedly in sequences of a few thousand frames such as for a regular XPCS experiment. The integration time for each speckle pattern is 1 ms, and the detector readout time is 0.29 ms (Ponchut *et al.*, 2011).

The recorded images are corrected to a flat-field image to reach a uniform quantum efficiency across the entire detector chip. Fig. 1(a) demonstrates a scattering pattern averaged over 2000 successive images. Since the detector is illuminated by an isotropic field of X-ray radiation, ensemble averages were calculated over pixels in iso- $q$  rings. Fig. 1(b) shows a waterfall plot of the photon count intensities of a collection of pixels within the circular region labeled in Fig. 1(a). The waterfall plot helps identify bad pixels, sample instability, misassignment of the direct beam position, or signs of radiation damage. It provides also a good intuitive support to predict the time-scale of the sample motion from the lifetime of the speckles. Since no sign of radiation damage was observed and the detector readout time is much shorter compared with the integration time, scattering patterns with longer integration time (*i.e.* multiples of 1 ms) were obtained by summing multiple sequential images pixel-by-pixel, and then used for the XSVS analysis.

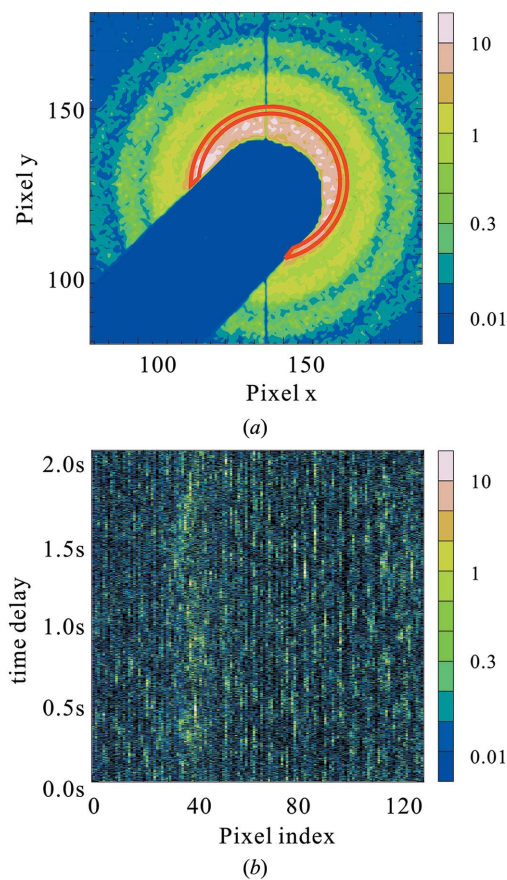


**Figure 1**

(a) Scattering pattern from a diluted silica colloidal suspension. The image is an average over 2000 measurements with 1 ms integration time. The dark shadow of the beam stop and the dark column in the scattering pattern were masked out for analysis. The rings schematically mark a collection of pixels at  $q = 2.95 \times 10^{-3} \text{ \AA}^{-1}$  with a width of  $\Delta q \simeq 1.0 \times 10^{-4} \text{ \AA}^{-1}$ . (b) Waterfall plot of the photon counts of pixels within the  $q$  ring labeled in (a). Color bars are shown as a visual aid.

### 4. Results

The contrast factor  $\beta(q, T)$  of the speckle patterns is extracted by the photon statistics analysis. The experimental probability density  $P(K)$  of detecting  $K$  photons is obtained by histogramming the photon counts over an ensemble of equivalent pixels and over a number of speckle patterns recorded with the same integration time  $T$  under the same illumination condition. The experimental  $P(K)$  is directly fitted with the negative-binomial distribution function by equation (11), with  $M$  and  $\langle K \rangle$  as adjustable parameters. Fig. 2 presents the photon probability density  $P(K)$  from experiments (markers) for four different integration times  $T$  of 1, 2, 4 and 8 ms. The fits with the negative-binomial distribution (solid lines in Fig. 2) match the experimental  $P(K)$  well throughout the entire range of  $K$  for all integration times. The fitted numbers of coherent modes  $M$  are 1.8, 3.4, 5.0 and 5.9, respectively, for the selected integration times, so that by equation (6) the contrast factors  $\beta(q, T)$  are 0.54, 0.30, 0.20 and 0.17. The beam coherence degenerates with the increase of the integration time  $T$ .

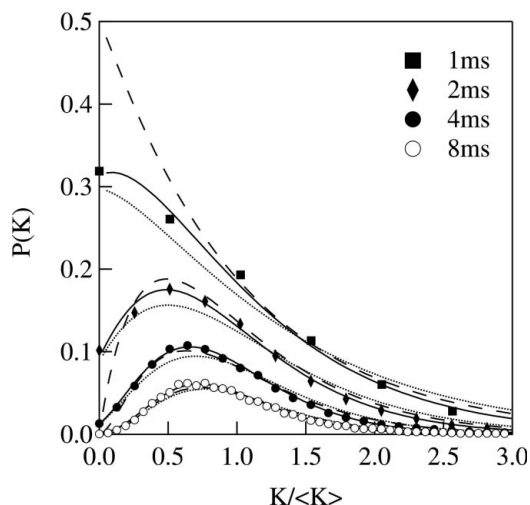


**Figure 2** Photon count statistics analysis performed over an ensemble of pixels marked in the circular region in Fig. 1(a) for four integration times. Markers represent the photon count probability density  $P(K)$  from the experiments, and solid lines are the fitting curves using the negative-binomial distribution function [equation (11)], dashed lines are the fitting curves using the gamma distribution function [equation (5)] and dotted lines are the fits using equation (11) with  $M$  as the only fitting parameter, while  $\langle K \rangle$  is calculated from the measured photon counts. The results are plotted as a function of reduced count  $K/\langle K \rangle$ , so that  $P(K)$  values with different integration times can be stacked in the same figure.

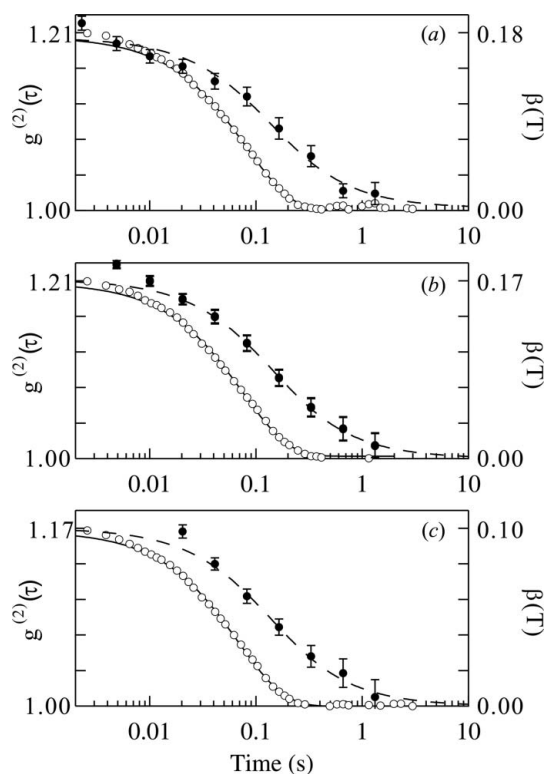
The background scattering from the kapton windows influences the contrast of the scattering patterns. The intensity is weak and Poisson distributed, so that it cannot be eliminated simply by subtracting it from the sample scattering patterns. However, it is a reasonable approach to reduce the Poisson signals of the background scattering by fitting with  $\langle K \rangle$  as a parameter. In Fig. 2, the calculated  $\langle K \rangle$  from the scattering intensity are 1.9, 3.9, 7.8 and 15.6 photons pixel<sup>-1</sup>. The fitted  $\langle K \rangle$  values, on the other hand, are 1.6, 3.5, 7.1 and 14.4 photons pixel<sup>-1</sup>. We explain this small systematic discrepancy as an effect of the background scattering from the kapton windows. Both approaches are adjusted to the best fit to the experimental  $P(K)$ . In Fig. 2, we show fits where both  $M$  and  $\langle K \rangle$  are left as adjustable parameters and, for comparison, fits where only  $M$  is an adjustable parameter. While both procedures lead to reasonably good fits, it is clear that fitting also for  $\langle K \rangle$  leads to better results in this case where the background scattering is non-negligible and difficult to quantify.

For comparison, fittings using the gamma distribution function by equation (5) are also shown, as dashed lines, in Fig. 2. The gamma distribution clearly fails to describe the  $P(K)$  values for low-scattering cases, and the discrepancy is, as expected, especially pronounced for the measurements with short integration times (e.g. 1 ms). As the integration time increases, the scattering patterns become more continuous and the wave-like property of the scattered X-rays dominates. The gamma distribution lineshape approaches that of the fitted negative-binomial distribution function (e.g. results for  $T = 8$  ms). Therefore, the gamma distribution is only conditionally applicable to speckle patterns with high scattering levels as

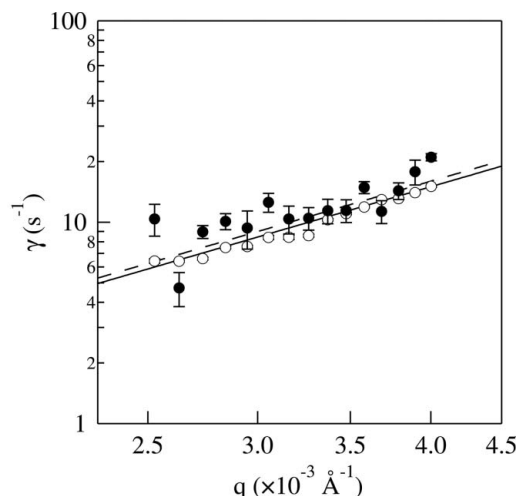
used in SVS with laser light scattering. In this work the negative-binomial distribution as a universal approach is used to fit the experimental  $P(K)$  for all integration times and over all iso- $q$  rings.

The contrast factors  $\beta(q, T)$  obtained from fitting the experimental  $P(K)$  with equation (11) for integration times that are  $2^n$  multiples of 1 ms, where  $n$  is an integer, are shown as solid markers in Figs. 3(a)–3(c) as a function of  $T$  for three different values of the momentum transfer  $q$ . These experimentally determined  $\beta(q, T)$  values are then modeled by equation (13) with three adjustable parameters  $\beta_1$ ,  $\beta_\infty$  and  $\gamma(q)$ , the last of which describes the relaxation rate associated with the sample motion. The fitted curves are shown as dashed lines in Figs. 3(a)–3(c) with the relaxation rate  $\gamma(q)$  to be (a)  $4.72 \pm 0.91$  s<sup>-1</sup>, (b)  $8.95 \pm 0.66$  s<sup>-1</sup> and (c)  $9.36 \pm 2.01$  s<sup>-1</sup>.

The same experimental data are also used to calculate the (XPCS) intensity autocorrelation  $g^{(2)}(q, \tau)$  from equation (1) over a sequence of 5000 successive scattering patterns, and averaged azimuthally over pixels in given iso- $q$  rings. The relaxation rate  $\gamma(q)$  is extracted by fitting  $g^{(2)}(q, \tau)$  with equation (3). Figs. 3(a)–3(c) also show the experimental (open markers) and the fitted (solid lines)  $g^{(2)}(q, \tau)$  as a function of time delay  $\tau$  for the same three iso- $q$  rings as in the XSVS



**Figure 3** Autocorrelation functions  $g^{(2)}(q, \tau)$  plotted as a function of the time delay  $\tau$  from the XPCS analysis and speckle contrast factors  $\beta(q, T)$  as a function of the integration time  $T$  from the XSVS analysis over three  $q$  rings of pixels (a) at  $q = 2.63 \times 10^{-3} \text{ \AA}^{-1}$ , (b) at  $q = 2.74 \times 10^{-3} \text{ \AA}^{-1}$  and (c) at  $q = 2.95 \times 10^{-3} \text{ \AA}^{-1}$ . The experimental  $g^{(2)}(q, \tau)$  (empty circles) are fitted by equation (3) (solid line) for the XPCS analysis. The experimental  $\beta(q, T)$  (filled circles) are fitted by equation (13) (dashed line) for the XSVS analysis. Note that the horizontal axis is labeled as ‘Time’ for simplicity but has different meanings for the two methods.


**Figure 4**

Relaxation rate  $\gamma(q)$  of the sample Brownian motion as a function of scattering vector  $q$  obtained by XPCS (empty circles) and XSVS (filled circles). Straight lines are fitted by equation (14) for XPCS (solid line) and for XSVS (dashed line).

analysis. The relaxation rate  $\gamma(q)$  obtained by XPCS analysis are (a)  $6.40 \pm 0.08 \text{ s}^{-1}$ , (b)  $6.60 \pm 0.10 \text{ s}^{-1}$  and (c)  $7.58 \pm 0.09 \text{ s}^{-1}$ .

The relaxation rates  $\gamma(q)$  obtained from XPCS (open markers) and XSVS (close markers) are compared for all  $q$  values in Fig. 4. The results from both methods match well within the experimental errors.

It should be noted that, while the XSVS results in Fig. 4 have larger statistical errors than the XPCS measurements, these can be reduced by repeating the experiment under the same illumination conditions (*e.g.* on a fresh location on the sample, if needed).

For Brownian samples, the diffusion coefficient  $D_0$  can be obtained by

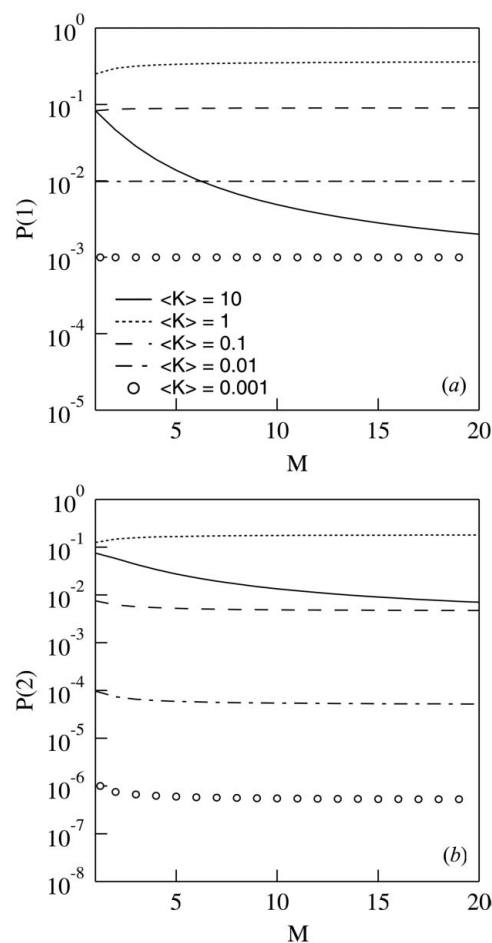
$$\gamma(q) = D_0 q^2. \quad (14)$$

The fact that the relaxation rates follow a quadratic dependence on the momentum transfer  $\gamma(q) \propto q^2$  demonstrates that the silica particles in PG undergo indeed a simple Brownian motion and hence the diffusion coefficient is obtained by fitting  $\gamma(q)$  as a linear function of  $q^2$ , with values  $D_0 = 9.99 \pm 1.75 \times 10^5 \text{ \AA}^2 \text{ s}^{-1}$  for XSVS (dashed line) and  $D_0 = 9.44 \pm 0.40 \times 10^5 \text{ \AA}^2 \text{ s}^{-1}$  for XPCS (solid line) (*c.f.* Fig. 4). The two values agree with each other within experimental error.

## 5. Discussion and conclusion

Similar to XPCS, XSVS is also a photon-starved technique. In this work the averaged count  $\langle K \rangle$  over rings of pixels varies from 0.6 photons  $\text{pixel}^{-1}$  to a few thousand photons  $\text{pixel}^{-1}$  for the XSVS analysis. The most important practical constraint for the photon statistical approach comes from the need of the experimental  $P(K)$  to have at least three points [*i.e.*  $P(0)$ ,  $P(1)$  and  $P(2)$ ] for the curve-fitting. This is somehow similar for XPCS where a (statistically significant) number of two photon

events are needed to calculate correlation functions. Once this condition is satisfied, there is no hard limit for the feasibility of the photon statistical approach. However, the possibility of using this approach still depends greatly on the scattering intensities  $\langle K \rangle$ . Fig. 5 shows the calculated probability densities of receiving 1 and 2 photons by using the negative-binomial distribution function with equation (11) as a function of  $M$  under various scattering levels: 10, 1, 0.1, 0.01 and 0.001 photons  $\text{pixel}^{-1}$ . In this work, 15 rings with 14–190 pixels were analyzed over 2048 patterns with the shortest integration time of  $T = 1 \text{ ms}$ . The largest number of sampling  $N$  for the photon statistics analysis is about  $4 \times 10^5$ . The feasibility of the measurement can be evaluated by  $P(1)$  and  $P(2)$  [particularly  $P(2)$ ]. In Fig. 5(b),  $P(2)$  at  $\langle K \rangle = 0.001$  photons  $\text{pixel}^{-1}$  lies in the  $10^{-6}$  range. For example, with the largest sampling size  $4 \times 10^5$  for our analysis, there is still less than one pixel receiving two photon counts. Hence, the photon statistics approach is not applicable at  $\langle K \rangle = 0.001$  photons  $\text{pixel}^{-1}$  or lower scattering levels.  $P(2)$  at  $\langle K \rangle = 0.01$  photons  $\text{pixel}^{-1}$  lies in the  $10^{-4}$  range. Only a few tens of pixels receive two photon counts. To improve the experimental statistics, the sampling size needs to be increased. However,  $P(2)$  at  $\langle K \rangle =$


**Figure 5**

Calculated probability density of receiving 1 and 2 photons. (a)  $P(1)$  and (b)  $P(2)$  with the negative-binomial distribution function by equation (11) under different scattering levels with  $\langle K \rangle = 0.001, 0.01, 0.1, 1.0$  and 10 photons  $\text{pixel}^{-1}$  as a function of the number of coherent modes  $M$ .

0.1 photons pixel<sup>-1</sup> lies in the 10<sup>-2</sup> range. A few thousand pixels receive two photons. Here, in a ring of pixels at  $q = 4.0 \times 10^{-3} \text{ \AA}^{-1}$  with  $\langle K \rangle = 0.58$  photons pixel<sup>-1</sup>, there are  $3.5 \times 10^4$  pixels receiving two photon counts. Under the current experimental conditions the contrast factor  $\beta$  should be able to be extracted from scattering patterns at the  $\langle K \rangle = 0.1$  photons pixel<sup>-1</sup> scattering level by using the photons statistics approach. From both Figs. 5(a) and 5(b) the probability densities  $P(1)$  and  $P(2)$  are much more sensitive to  $\langle K \rangle$  than to the number of coherence modes  $M$  at low scattering levels  $\langle K \rangle < 1$ . Hence, the number of samplings can be evaluated based on the scattering level  $\langle K \rangle$ .

The accuracy of contrast factor  $\beta$  is greatly influenced by the detection noise, especially at low scattering levels. According to equation (12), the Poisson noise can introduce a maximum of detection error of  $1/\langle K \rangle$ . At low scattering cases, for example  $\langle K \rangle < 1$ , the Poisson error  $1/\langle K \rangle$  is larger than 1. The contrast factor  $\beta$  has a value between 0 and 1 by definition. Therefore, the error introduced by Poisson noise is larger than 100% of the contrast factor. The signal-to-noise ratio can be increased by repeating the experiment.

As reported by DeCaro *et al.* (2013), judging by the  $1/e$  point of  $g^{(2)}(q, t)$  and  $\beta(q, T)$  at the same  $q$ , the XSVS method is 20 times more sensitive than the XPCS method under the same detector repetition rate. However, the XSVS method is not limited by the detector repetition rate. The integration time  $T$  can be reduced even further, for example by using a (mechanical or electronic) shutter. Hence, XSVS is capable of studying faster dynamics. However, based on the previous discussion, the time window of XSVS is limited by the scattering level  $\langle K \rangle$ . The possibility of receiving two photons  $P(2)$  should be calculated based on  $\langle K \rangle$ , and the number of samplings should be evaluated judging by  $P(2)$ .

Our results show that the quantum statistical model for the scattering from a partially coherent source described by the negative-binomial distribution function works remarkably well for the XSVS analysis. The problem then relies on how to interpret the quantal measure (*i.e.*  $K$ ) from the detection results, which is detector dependent. The photon-counting detectors are preferred because of their fast readout rate, having zero electronic noise, and most importantly the direct reading of photon counts  $K$  (Radicci *et al.*, 2012; Ponchut *et al.*, 2011). In addition, with pixelated photon-counting detectors it is highly unlikely to have charge-sharing problems like CCD detectors have. However, when the X-rays impinge on the border of neighboring pixels, depending on the exact thresholding scheme, there is a finite probability that a photon is mis-assigned or doubly counted. Random errors such as this can be reduced by repeating the experiment to have better sampling of the photon counts  $K(T)$ . Newly developed pixelated detectors such as the Medipix3 family (Gimenez *et al.*, 2011; Ballabriga *et al.*, 2013) enable the communication of adjacent pixels, which further reduces the risk of assigning photons to the wrong pixels. These new photon-counting detectors are ideal for XSVS, as demonstrated by the photon statistics approach proposed in this paper.

This work demonstrates the feasibility of the speckle statistics approach to speckle visibility experiments by making a direct comparison between XSVS and XPCS results using third-generation synchrotron radiation sources. In this situation the XSVS data series can be constructed by time binning frames recorded in an XPCS experiment. The analysis from both methods will provide identical results if the detector readout time is negligible in comparison with the acquisition time. However, the main motivation for XSVS is to enable measurements where XPCS does not work. Pushing the limits of the phase space that can be explored by coherent scattering towards even faster times, reaching perhaps timescales of the order of microseconds is, for instance, one of the main motivations behind building instruments such as the Coherent Hard X-ray beamline at the NSLS-II (Fluerasu *et al.*, 2011). Since the present detector technology is not yet at a level where frame repetition rates of 1 MHz are possible, accessing such timescales is not possible with XPCS. On the other hand, XSVS does not require such repetition rates but only the capabilities of controlling the exposure (integration) time to this resolution, a feature that modern pixelated detectors have already accomplished. XSVS can also present important benefits in terms of reducing artifacts associated with beam damage, one of the main problems in the study of soft and biological materials. Even though the longest integration times required by XSVS are longer than the integration times of individual frames in a XPCS series, the total dose at any given location on the sample can be smaller. This is particularly useful if the dose can be distributed over different samples or over different locations across the sample. The error bars on any measurement can then be reduced by simply repeating nominally the same experiment on a fresh sample, a feature shared, for example, with many high-energy experiments, but not with XPCS. The fact that separate measurements are performed for different integration times also opens new possibilities such as increasing the beam attenuation (and hence reducing the beam damage) only for the longer integration times, while using the entire available flux and maximizing signal-to-noise ratio for the shorter integration times.

In conclusion, here we demonstrate the photon statistics approach to X-ray speckle visibility spectroscopy by studying the coherent X-ray scattering from a dilute colloidal suspension of hard-sphere-like silica particles. The contrast factor of single speckle patterns is obtained by fitting the experimental probability density  $P(K)$  of photon counts with the negative-binomial distribution, which is then used to extract the dynamic information of the sample. The results from the XSVS analysis are in excellent agreement with those obtained by the well established XPCS method, and open exciting new possibilities for studies of fast dynamics or experiments with beam-sensitive soft and biological materials focusing at the new third-generation synchrotron sources.

The authors would like to thank the ESRF ID10 beamline for the beam time, and Y. Chushkin and F. Zontone for the support during the experiments. The research is financially

supported by NSLS-II under contract No. DE-AC02-98CH10886 with the US Department of Energy, and Brookhaven National Laboratory Directed Research Development (LDRD) No. 11-025.

## References

- Ballabriga, R., Aloyz, J., Blaj, G., Campbell, M., Fiederle, M., Frojdh, E., Heijne, E. H. M., Llopart, X., Pichotka, M., Procz, S., Tlustos, L. & Wong, W. (2013). *J. Instrum.* **8**, C02016.
- Bandyopadhyay, R., Gittings, A. S., Suh, S. S., Dixon, P. K. & Durian, D. J. (2005). *Rev. Sci. Instrum.* **76**, 093110.
- DeCaro, C., Karunaratne, V. N., Bera, S., Lurio, L. B., Sandy, A. R., Narayanan, S., Sutton, M., Winans, J., Duffin, K., Lehuta, J. & Karonis, N. (2013). *J. Synchrotron Rad.* **20**, 332–338.
- Dixon, P. K. & Durian, D. J. (2003). *Phys. Rev. Lett.* **90**, 184302.
- Fluerasu, A., Chubar, O., Kaznatcheev, K., Balster, J., Wiegart, L., Evans-Lutterodt, K., Carlucci-Dayton, M. & Berman, L. (2011). *Proc. SPIE*, **8141**, 81410J.
- Gimenez, E. N., Ballabriga, R., Campbell, M., Horswell, I., Llopart, X., Marchal, J., Sawhney, K. J. S., Tartoni, N. & Turecek, D. (2011). *IEEE Trans. Nucl. Sci.* **58**, 323–332.
- Goodman, J. W. (2007). *Speckle Phenomena in Optics: Theory and Applications*. Englewood: Roberts and Company.
- Grübel, G., Madsen, A. & Robert, A. (2008). *Soft-Matter Characterization*, edited by R. Borsali & R. Pecora, ch. 18, pp. 953–995. Berlin: Springer-Verlag.
- Hruszkewycz, S. O., Sutton, M., Fuoss, P. H., Adams, B., Rosenkranz, S., Ludwig, K. F., Roseker, W., Fritz, D., Cammarata, M., Zhu, D., Lee, S., Lemke, H., Gutt, C., Robert, A., Grübel, G. & Stephenson, G. B. (2012). *Phys. Rev. Lett.* **109**, 185502.
- Inoue, I., Shinohara, Y., Watanabe, A. & Amemiya, Y. (2012). *Opt. Express*, **20**, 26878–26887.
- Lee, S. *et al.* (2013). *Opt. Express*, **21**, 24647–24664.
- Mandel, L. (1958). *Proc. Phys. Soc.* **72**, 1037.
- Mandel, L. (1959). *Proc. Phys. Soc.* **74**, 233.
- Orsi, D., Fluerasu, A., Moussaïd, A., Zontone, F., Cristofolini, L. & Madsen, A. (2012). *Phys. Rev. E*, **85**, 011402.
- Ponchut, C., Rigal, J. M., Clément, J., Papillon, E., Homs, A. & Petitdemange, S. (2011). *J. Instrum.* **6**, C01069.
- Radici, V., Bergamaschi, A., Dinapoli, R., Greiffenberg, D., Henrich, B., Johnson, I., Mozzanica, A., Schmitt, B. & Shi, X. (2012). *J. Instrum.* **7**, C02019.
- Sikharulidze, I., Dolbnya, I. P., Fera, A., Madsen, A., Ostrovskii, B. I. & de Jeu, W. H. (2002). *Phys. Rev. Lett.* **88**, 115503.
- Sutton, M. (2008). *C. R. Phys.* **9**, 657–667.
- Sutton, M., Laaziri, K., Livet, F. & Bley, F. (2003). *Opt. Express*, **11**, 2268–2277.
- Sutton, M., Mochrie, S. G. J., Greytak, T., Nagler, S. E., Berman, L. E., Held, G. A. & Stephenson, G. B. (1991). *Nature (London)*, **352**, 608–610.